Chinese Chemical Letters 32 (2021) 3579–3583

Contents lists available at ScienceDirect

Chinese Chemical Letters

journal homepage: www.elsevier.com/locate/cclet

Communication

Surface oxidized iron-nickel nanorods anchoring on graphene architectures for oxygen evolution reaction

Xu Yu*, Zhixin Zhao, Chengang Pei

School of Chemistry and Chemical Engineering, Yangzhou University, Yangzhou 225000, China

ARTICLE INFO

Article history:
Received 17 February 2021
Received in revised form 9 March 2021
Accepted 15 March 2021
Available online 17 March 2021

Keywords:
Architectures
Graphene oxides
FeNi nanorods
Metallic oxide
Oxygen evolution reaction

ABSTRACT

Surface oxidized iron-nickel nanorods coupling with reduced graphene architectures (FeNi-O-rGA) are successfully constructed *via* hydrothermal, freeze-drying, and thermal activation approaches. The hierarchical structure can provide lots of pathways for fast ion diffusion and charge transfer, and expose abundant catalytic sites. Meanwhile, the activity of FeNi-O-rGA is boosted by the optimized metal-oxygen bond strength in $FeNi_3$ alloys. Partial oxidized FeNi nanorods are strongly coupled with rGA by the formation of metal-O-C bonds, which can impede the aggregation of $FeNi_3$ alloys and increase the utilization of active sites. The special structure and partially oxidized FeNi nanorods for FeNi-O-rGA can result in excellent OER activity and catalytic stability. Only 215 mV of overpotential is required to drive the current density of 10 mA/cm^2 as well as the Tafel slope of 50.9 mV/dec in 1 mol/L KOH. The change of surface chemistry of FeNi-O-rGA is confirmed by XPS after the OER test, which indicates the highly catalytic stability of FeNi-O-rGA due to the formation of intermediate metal oxyhydroxide.

Exploring renewable energy sources is accepted as an effective strategy to satisfy the fast growth of energy demand as well as alleviate the consumption pressure of fossil fuels [1,2]. Oxygen evolution reaction (OER), as a direct electrochemical oxidation process of water-splitting, can provide a clean and long-term energy source by converting the energy modality due to their high overall efficiency [3,4]. However, the sluggish kinetics for OER is still the bottleneck for the entire process of electrolytic water-splitting, resulting from the four-electron process by consuming hydroxyl ions or water molecules at the anode [5–9]. Iridium oxide (IrO_2) and ruthenium dioxide (RuO_2) are known to show excellent OER activities [6,10,11], such as low overpotential and high durable stability, but the scarcity of resources and high prices restrict their applications in a large-scale system [12]. Therefore, the development of highly active non-precious catalysts with the enhanced OER activity is urgent to solve this issue.

Recently, cheap transition metal-based OER catalysts, such as Fe, Co, Ni, have been regarded as effective alternative materials to show the modest catalytic activity [13], which is generally determined by exposing amounts of the active sites and the activity of active sites. By synergistically controlling the morphological structure and surface chemical states, the OER performance of Fe- and Ni-based catalysts can be significantly improved in comparison to RuO_2 and IrO_2 [14–16]. The activity of catalytic sites is related to the electronic structure of catalysts. It is reported that surface metal cations are believed to be the active sites for OER [17]. The reaction proceeds through a series of intermediates bound by metal-oxygen (M–O) bond, and the relationship between M–O bond strength and catalytic activity is studied [5]. While the M–O bond strength should be optimized for active catalysts neither too strong nor too weak, and the active M–O bond strength presented at the top of the 'volcano map'. Lyons *et al.* demonstrated the experimental activity trend of metals in an alkaline electrolyte (Ni > Co > Fe) [18], and Delahay *et al.* reported the OER overpotential trend at 1 A/cm^2 (Ni < Fe < Co) [19,20], which are related to M–OH strength [21]. Fe-Ni compounds have been proved to show the enhanced OER activity by the coordination of Fe at the Ni sites [22–25]. However, the catalytic activity is still restricted by their low conductivity and stability resulting from the aggregation and corrosion of active materials in alkaline electrolytes.

In addition to the compositional control, the design of the morphological structure of catalysts is important to provide abundant channels for fast electrolyte diffusion and expose more active sites for compact contact of electrode/electrolyte. The deposition of FeNi compounds on carbon matrix (carbon nanotube, graphitic carbon, *etc.*) has been demonstrated to show the enhanced OER activity due to the increased conductivity [26]. Reduced graphene architectures (rGA), self-assembled by the π-π interaction of graphene oxide

* Corresponding author.
E-mail address: yxypz15@yzu.edu.cn (X. Yu).

https://doi.org/10.1016/j.cclet.2021.03.040

nanosheets, can show the hierarchical structure and act as a conductive host to improve the conductivity and stability of transition metal-based catalysts for OER [27]. Meanwhile, the surface functional groups (hydroxyl, carboxyl) are beneficial to form the M–O-C bonds at the metal/graphene interfaces, which can guarantee the stability of catalysts during the OER test. However, FeNi compounds uniformly coupled on graphene architecture as effective catalysts for OER still face challenges.

Herein, we reported a surface oxidized iron-nickel nanorods coupling on rGA (FeNi-O-rGA) by combining hydrothermal, freeze-drying, and thermal activations. FeNi nanorods are *in-situ* grown on graphene surface during the hydrothermal process and subsequently formed the oxidized states at FeNi nanorods surface after thermal activation, predicting the improved stability of FeNi-O-rGA for OER. As probed by a series of microscopic and spectroscopic technologies, FeNi nanorods with uniform size and partial oxidation are uniformly distributed on graphene surfaces without aggregation. FeNi-O-rGA exhibited superior OER catalytic performance to Fe-O-rGA, Ni-O-rGA, and IrO_2/C, including low overpotential to drive the current density of 10 mA/cm^2, small Tafel slope, and long-term stability after 1000 cycles, which can be attributed to the synergistic effect of hierarchical structure and modified surface chemistry.

As illustrated in Fig. 1a, FeNi-O-rGA was *in-situ* synthesized by a one-step hydrothermal approach following the thermal activation. In brief, the homogeneous solution of metal precursors, oxalic acid, and graphene oxides is important to construct the hierarchical structure with uniform distribution of nanorods. The graphene architectures and FeNi nanorods are *in-situ* formed during the hydrothermal process. Generally, the graphene architecture is formed by the self-assembly of graphene nanosheets through π-π configuration and the formation of hydrogen bonding. Meanwhile, we also anticipate that the FeNi nanorods incorporate with graphene oxide due to the electrostatic force between the oxygen-containing groups of GO and the surface oxidation state of nanorods. As further treatment by a freeze-drying method and thermal activation, the macroscopic structure cylinder FeNi-O-rGA can well remain with small size demolition (Fig. S1 in Supporting information), and the spindly FeNi nanorods are also oxidized during the decomposition of functional groups from graphene oxides.

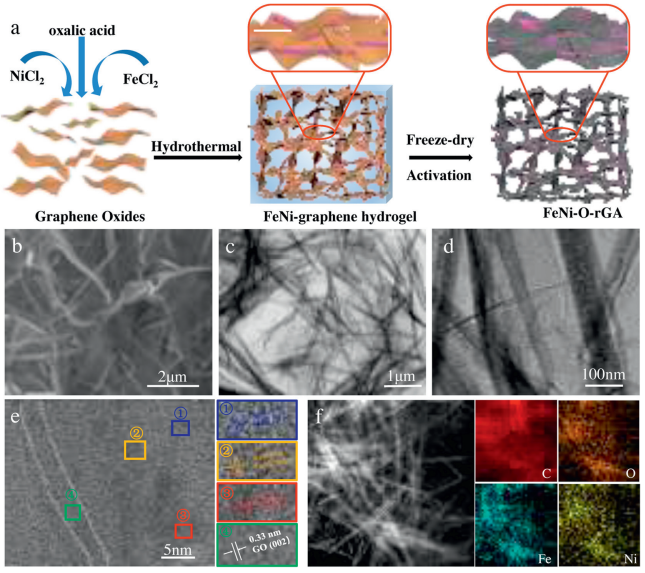

Fig. 1. (a) The synthetic scheme of FeNi-O-rGA. (b) SEM, (c,d) TEM images, (e) HR-TEM and HR-TEM images, (f) STEM image and the related elemental (C, O, Fe and Ni) mapping.

The morphology and structure of FeNi-O-rGA were characterized by scanning electron microscope (SEM). Fig. 1b and Fig. S2a (Supporting information) are the SEM image of FeNi-O-rGA. It was observed that FeNi-O-rGA possesses the hierarchical structure, and the surface oxidized FeNi nanorods are uniformly distributed on microporous walls in direct contact with graphene. Transmission electron microscope (TEM) further revealed that FeNi-O-rGA owns the shrink graphene lattices and uniform nanorods distribution with an average length of 2 μm and width of 40 nm; no aggregated phenomena can be observed even after high-temperature treatment attributing to the existence of FeNi nanorods inhibits the restacking of GO (Fig. 1c). The rough surface for FeNi nanorods induces by the surface oxidation and the hybridization with graphene nanosheets (Fig. 1d). The stabilized FeNi nanorods are ascribed to the strong coupling of oxidized surface of FeNi with graphene and the formation of strong covalent bond interaction *via* condensation reaction during the thermal treatment. As the high-resolution TEM is shown in Fig. 1e, the interplanar distances of lattice fringes are 0.25 and 0.29 nm corresponding to the (311) and (220) plane of the Fe_2O_3, the d-spacing of 0.21 nm and 0.33 nm correspond to the (111) plane of $FeNi_3$ and (002) plane of graphene. The polycrystalline characteristic of FeNi-O-rGA was further confirmed by the selected area electron diffraction (SAED) pattern, the large diameter diffraction aperture is corresponding to the $FeNi_3$ (200) plane, and the other is corresponding to (111) plane of $FeNi_3$ (Fig. S2b in Supporting information). The energy dispersive spectroscopy (EDS) displays the obvious peaks implying the existence of C, O, Fe and Ni elements (Fig. S3 and Table S1 in Supporting information). The uniform distribution of all elements is further confirmed by elemental mapping in Fig. 1f. The outline of neatly distributed Fe and Ni elements well matches with the shape of nanorods, implying the successful synthesis of nanorods on graphene architectures.

The phase composition and crystallinity of the FeNi-O-rGA were characterized by X-ray diffraction (XRD) in Fig. 2a and Fig. S4 (Supporting information). It can be observed that the peak approximately at 26.38° for GA and 26.28° for FeNi-O-rGA owing to the (002) plane of graphitic carbon, suggesting the successful reduction of graphene oxides [28]. The two broad peaks imply the highly amorphous phase of rGA, and the slight peak shift can be attributed to the change of interlayer distance of graphene by hybridization with FeNi nanorods. FeNi-O-rGA shows a series of clear diffraction peaks. The peaks centering at 44.2°, 52.0° and

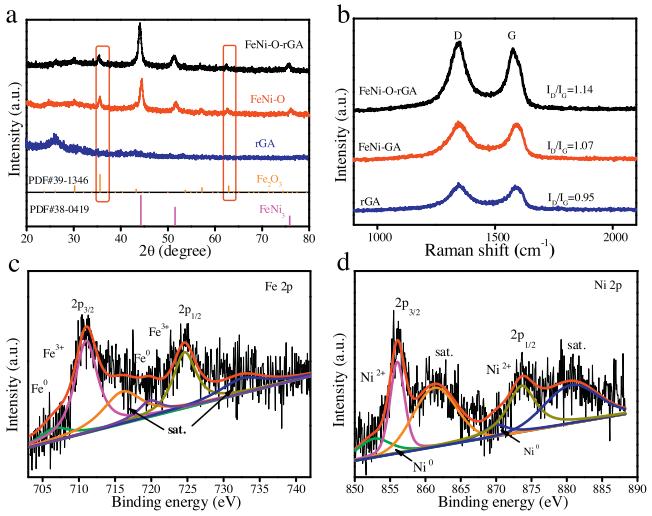

Fig. 2. (a) XRD patterns of the rGA, FeNi-O nanorod and FeNi-O-rGA. (b) Raman spectra of the rGA, FeNi-GA and FeNi-O-rGA. High magnification XPS spectra of (c) Fe 2p and (d) Ni 2p.

75.7° correspond to the (111), (200), and (220) crystal planes of $FeNi_3$ alloys (PDF#38-0419), respectively. Some weak peaks are located at 30.2° and 35.4° attributing to the (220) and (311) planes of Fe_2O_3 (PDF#39-1346), and the effect of activation temperature on the content of Fe_2O_3 is confirmed by XRD (Fig. S5 in Supporting information). These results confirm that FeNi-O-rGA contains not only $FeNi_3$ alloys but also the oxidized state of Fe formed during the thermal activation process. Furthermore, the structural change of FeNi-O-rGA was elucidated by Raman in Fig. 2b. Two typical peaks at 1344 and 1582 cm^{-1} assign to the defective structure of graphene lattices (D band) and the stretchable bonding of sp^2 carbons (G band) [29]. FeNi-O-rGA exhibits a red-shift of the G band, which can be attributed to stretchable carbon-carbon bond during the reduction process of graphene oxides and the formation of metal-O-C bond at graphene/FeNi nanorods interfaces [30,31]. The degree of structure distortion is evaluated by the intensity ratio of the D band and G band (I_D/I_G). The value of I_D/I_G for FeNi-O-rGA (1.14) is larger than that of GA (0.95), implying the increased defective density in the hierarchical structure due to the coupling of metal oxide with graphene.

X-ray photoelectron spectroscopy (XPS) was probed to analyze the surface composition and elemental states of FeNi-O-rGA, which demonstrates the existence of. C, O, Fe and Ni elements from the full scan XPS spectra (Fig. S6a and Table S2 in Supporting information). Fig. S6b (Supporting information) shows the high-resolution C 1s spectra of FeNi-O-rGA. Three fitted peaks centering at 284.7 eV, 285.7 eV, and 288.4 eV correspond to the C-C, C-O, and C=O, respectively. The O 1s peak was divided into four major peaks at 530.3 eV, 531.5 eV and 532.9 eV, in accordance with metal-O, metal-O-C and C—O configurations, respectively (Fig. S6c in Supporting information). The high content of defective oxygen coordination on the surface of FeNi-O-rGA can modulate the oxidation kinetics to improve the OER properties. To imply the boosted activity, the interaction between Fe and Ni for FeNi-O-rGA is confirmed by Fe 2p and Ni 2p spectra. Fig. 2c shows the typical peaks of Fe 2p, the peaks at 706.6 eV and 719.8 eV are attributed to Fe°, which is an account for the reduction of Fe^{2+}, and the peaks at 711.1 eV and 724.6 eV with the satellite peaks at 716.3 eV and 733.1 eV are indexed to Fe^{3+}; while the separation of 2p doublet was 13.7 eV, which is a typical feature of Fe_2O_3 [32,33]. As proved by lectures, the electrochemical activity for OER can be improved by the incorporation of Fe^{3+} [34,35]. The peaks at 852.5 eV and 869.6 eV indicate the existence of Ni° (Fig. 2d). And the peak at 855.9 eV and 877.6 eV can be assigned to Ni^{2+} with the related satellite peaks at 861.4 eV and 873.7 eV. Above all, this phenomenon indicates a large content of metallic Fe and Ni on the surface of the nanocomposites. And the existence of Fe^{3+} and Ni^{2+} may derive from the fact that the $FeNi_3$ alloys were active metals and their surface would be oxidized with the oxygen group during the reduced process of the GO. The oxidized states of Fe and Ni indicate the surface oxidation of $FeNi_3$ alloys, which is consistent with the XRD result. The conversion of Ni^{2+} to Ni^{3+} during the catalytic process as the electroactive sites for OER operation, which has a significant effect on the electrocatalytic activity [36,37]. Furthermore, the high ratio of Fe^{3+} and Ni^{2+} for FeNi-O-rGA is shown by integrating the fitted peak area from related XPS spectra. The surface oxidized FeNi alloys as the dominant active sites can effectively improve the efficiency of hydroxyl adsorption and oxyhydroxide formation, predicting the good electrocatalytic activity of FeNi-O-rGA during the OER test.

The electrocatalytic activity of FeNi-O-rGA, Ni-O-rGA and Fe-O-rGA for OER was initially evaluated by linear sweep voltammetry (LSV) measurement at a scan rate of 5 mV/s. The catalyst is activated and stabilized by cyclic voltammetry (CV). As is shown by the polarization curve (Fig. 3a), a typical peak at 1.32 V corresponds to Ni-based catalysts for OER, implying the conversion between Ni^{2+} and Ni^{3+} [31]. The LSV curves for FeNi-O-rGA exhibit the best catalytic activity in contrast to the control sample and commercial IrO_2/C catalyst. The overpotentials for all catalysts at the catalytic current density of 10 mA/cm^2 are compared, as shown in Fig. 3a. To derive the high current density of 10 mA/cm^2, the required overpotential of FeNi-O-rGA is only 215 mV, which is much lower than that of Ni-O-rGA (340 mV), Fe-O-rGA (400 mV), commercial IrO_2/C (320 mV) and the recently reported Ni-based OER catalysts (Table S3 in Supporting information). Meanwhile, the change of reduction peak for FeNi-O-rGA caused by the incorporation of Fe into Ni sites, which can elucidate the superior catalytic activity of FeNi-O-rGA to the control catalysts. The catalytic activity of the

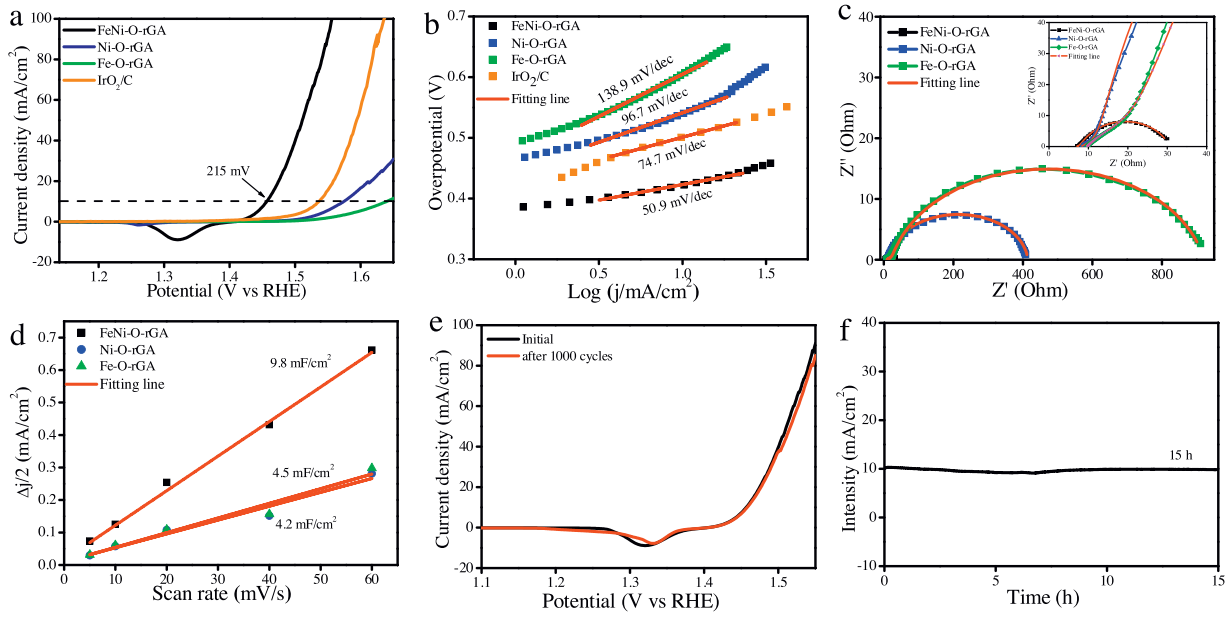

Fig. 3. (a) The polarization curves and (b) Tafel plots of FeNi-O-rGA, Ni-O-rGA, Fe-O-rGA and IrO_2/C catalysts. (c) Nyquist plots and (d) the capacitive current *versus* the scan rate of FeNi-O-rGA, Ni-O-rGA and Fe-O-rGA. (e) The polarization curves of FeNi-O-rGA at the 1st and 1000th CV cycles. (f) Chronoamperometry measurement of FeNi-O-rGA at the potential of 1.46 V.

optimal ratio of metal ions anchoring on graphene architectures is compared, and FeNi-O-rGA is best for OER (Fig. S7 in Supporting information). When the content of metal ions in catalysts is over optimal composition, the OER activity decreases owing to the poor conductivity of the excessive metal oxides. Meanwhile, FeNi-O-rGA is thermally activated at different temperatures and the corresponded electrochemical performance is compared (Fig. S8 in Supporting information). At the temperature of 400 °C, FeNi-O-rGA shows the lowest overpotential to reach the current density of 10 mA/cm^2 due to the optimal composition of metal oxides. The hierarchical structure can provide abundant ion transport pathways and expose more effective active sites, and the formation of covalent bonds between FeNi nanorods and GA are favorable for improving the stability of ion adsorption in the alkaline electrolyte during the OER test.

Tafel slope is an important index to verify the electrocatalytic kinetics of the catalysts at a low potential. As shown in Fig. 3b, the Tafel slope of FeNi-O-rGA (50.9 mV/dec) is lower than that of Ni-O-rGA (96.7 mV/dec), Fe-O-rGA (138.9 mV/dec) and IrO_2/C (74.7 mV/dec), suggesting the low activation energy for FeNi-O-rGA to drive an overpotential for OER. Electrochemical impedance spectroscopy (EIS) was employed to evaluate the interfacial behaviors of all catalysts and the equivalent circuit of the electrochemical process is shown in Fig. S9 (Supporting information). Fig. 3c shows the Nyquist plot of the catalysts, and the semicircle represents the charge transfer resistance (R_{ct}) at the electrolyte/electrode interface or inner the electrode. FeNi-O-rGA shows a smaller diameter of a semicircle and a lower R_{ct} value (21.3 Ω) than that of Ni-O-rGA (398 Ω) and Fe-O-rGA (899 Ω), implying the high activity and fast kinetics of FeNi-O-rGA for OER.

To investigate the enhanced electrocatalytic activity for FeNi-O-rGA, the electrochemical surface area (ECSA) is estimated. The CV curves of all catalysts were measured at the given potential window without faradic reaction. The value of ECSA is proportional to the double-layer capacitance (C_{dl}), which can be calculated by fitting the linear plot of the capacitive current versus the scan rates from CV curves (Fig. S10 in Supporting information). The larger C_{dl} value for FeNi-O-rGA (9.8 mF/cm^2) than that of Fe-O-rGA (4.5 mF/cm^2) and Ni-O-rGA (4.2 mF/cm^2) implies the increased electrochemical surface area, which can expose more efficient active sites for fast OER operation (Fig. 3d). Besides, the ECSA was also calculated (Table S4 in Supporting information) and FeNi-O-rGA owns the highest ECSA (17.15 mA/cm^2). The specific activity is obtained by normalizing the apparent current to ECSA (Fig. S11a in Supporting information). The FeNi-O-rGA shows the highest catalytic efficiency of 0.164 mA/cm^2 at 1.5 V, which is about 12 times of Ni-O-rGA (0.013 mA/cm^2) and 23 times of FeNi-O-rGA (0.007 mA/cm^2). The turnover frequency (TOF) was calculated to evaluate the intrinsic electrocatalytic activity of FeNi-O-rGA by assuming all Fe and Ni ions as the active sites (Fig. S11b in Supporting information). FeNi-O-rGA possesses the highest TOF value at the given overpotential indicating the high catalytic activity, which is consistent with specific activity (Fig. S9). At the overpotential of 215 mV, the TOF value for FeNi-O-rGA (0.06 s^{-1}) is 7.6 and 25 times higher than Ni-O-rGA (0.0078 s^{-1}) and Fe-O-rGA (0.0024 s^{-1}). Therefore, it can be concluded that the formation of Fe-Ni hydroxide/oxyhydroxide layer on FeNi alloys surface can increase the electroactive surface area, accelerate the charge transfer and reduce the contact resistance between electrode and electrolyte during the OER test.

Except for the high catalytic activity, the long-life durability is another significant concern to evaluate the catalysts in practical application. The catalytic durability of FeNi-O-rGA is measured by CV curves and chronoamperometric (CA). After a continuous scan for 1000 cycles, the polarization curves for FeNi-O-rGA is well overlapped with its initial cycle (Fig. 3e). It is observed that the reduction peak of Ni^{2+}/Ni^{3+} is slightly blue-shifted by the anion coordination around the transition metal center. The overpotential is nearly no skewing to reach the current density of 10 mA/cm^2 and slightly increased from 260 mV for the initial cycle to 265 mV for the 1000th cycle to obtain the current density of 40 mA/cm^2, indicating the superior catalytic durability for FeNi-O-rGA. Furthermore, the CA is measured at the given potential of 1.46 V (10 mA/cm^2) for 15 h in Fig. 3f. The negligible change of current density implies that FeNi-O-rGA is highly active with stable electrocatalytic behaviors.

The abovementioned physical characterization and electrochemical behaviors demonstrate that FeNi-O-rGA shows the hierarchical structure and excellent catalytic performance for OER reaction, which could be ascribed to the following reasons: 1) graphene architecture improves not only the electrical conductivity but also the stability of FeNi nanorods by the electrostatic interaction. 2) The hierarchical structure can increase the surface area by exposing more efficient catalytic active sites for OER and provide abundant pathways for fast ion diffusion and charge transfer. 3) The surface oxidation on FeNi nanorods, especially during the electrochemical activation in alkaline electrolyte, can improve the surface hydrophilicity and promote the formation of electroactive sites for OER. 4) The Fe incorporation can optimize the surface chemistry of FeNi nanorod to enhance the kinetics behaviors for OER, like the smaller Tafel and R_{ct} values. 5) The strong coupling of FeNi nanorods with graphene architectures can significantly improve the catalytic stability of FeNi-O-GA, as demonstrated by CA after 15 h in alkaline electrolyte.

The change of surface morphology and chemical states of FeNi-O-rGA after the OER test for 15 h were evaluated by TEM, XRD, and XPS in Fig. 4. Fig. 4a shows the well-maintained nanorod structure, and the rough surface corresponds to the surface oxidation during the OER process. The lattice fringe for FeNi nanorods and the boundary at graphene/FeNi nanorods interface is more obscure than the initial state, attributing to the further electro-oxidation and the conversion of intermediate metal oxyhydroxide. As is further confirmed by XRD spectra (Fig. 4b), the strong typical XRD patterns of FeNi alloys become much weak after the OER test, and some of the original weak patterns disappear, implying the weak polycrystalline characteristic with the formation of amorphous

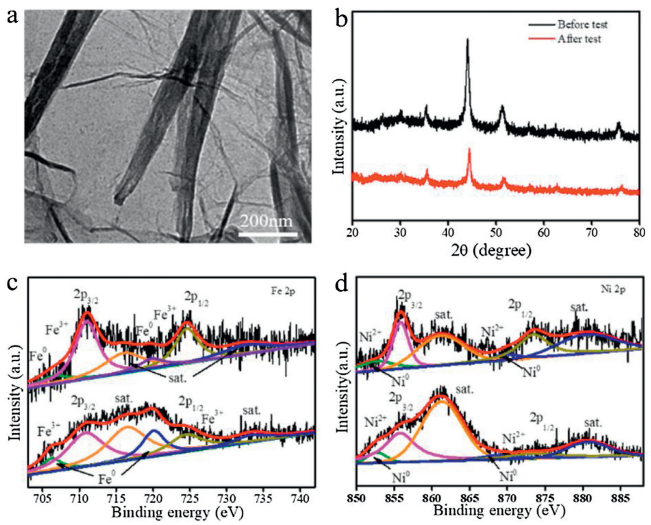

Fig. 4. (a) TEM image of FeNi-O-rGA after 1000 CV curves. (b) XRD of FeNi-O-rGA before and after OER test. XPS spectra of (c) Fe 2p and (d) Ni 2p for FeNi-O-rGA after OER test.

structure. A little peak shift for FeNi-O-rGA after the OER test is ascribed to the formation of intermediate metal oxyhydroxide. These features strongly confirmed the good catalytic stability for FeNi-O-rGA. XPS analysis was also carried out on the samples after the electrochemical test. The appearance of C–F bond in C 1s spectra and O—F bond in O 1s spectra is from the residual binder (Fig. S12 in Supporting information). By comparison, the change of XPS spectra is ascribed to the further oxidation and formation of metal oxyhydroxide on graphene nanosheet, which is caused by the intermetallic forces to make the electronic structure more stable (Figs. 4c and d).

In conclusion, we successfully fabricated the hierarchically structured FeNi-O-rGA catalyst for OER *via* hydrothermal and thermal activation. The partial oxidation of FeNi nanorods was *in-situ* grown on graphene surface during the treatment, which is favorable to increase the electrical conductivity and stability of FeNi-O-rGA catalyst. The surface oxidation of FeNi nanorods can provide abundant active sites. Due to the hierarchical structure and the boosted activity by Fe incorporation, FeNi-O-rGA exhibited an excellent catalytic activity for OER. To derive the current density of 10 mA/cm^2, FeNi-O-rGA required a low overpotential of 215 mV. The CA result confirmed that FeNi-O-rGA showed highly catalytic stability, and the change of surface morphology and chemical states were confirmed by various microscopic and spectroscopic analyses. This method can provide an effective strategy to construct the graphene architectures with coupling transition-metal based catalysts for OER.

Declaration of competing interest

The authors declare that they have no known competing financial interests or personal relationships that could have appeared to influence the work reported in this paper.

Acknowledgments

The work is supported by the National Natural Science Foundation of China (No. 21805239); the Natural Science Foundation of the Jiangsu Higher Education Institutions of China (No. 18KJB150034); 'Six Talent Peaks Project' in Jiangsu Province (No. XCL-104); 'High-End Talent Project' of Yangzhou University, and the 'Lvyang Jinfeng' Talents Attracting Plan. We also acknowledge the technical support at the Testing Center of Yangzhou University.

Appendix A. Supplementary data

Supplementary material related to this article can be found, in the online version, at doi:https://doi.org/10.1016/j.cclet.2021.03.040.

References

[1] G. Zhang, G. Wang, H. Liu, J. Qu, J. Li, Nano Energy 43 (2018) 359–367.
[2] K.G. dos Santos, C.T. Eckert, E. De Rossi, et al., Renew. Sustain. Energy Rev. 68 (2017) 563–571.
[3] B. Lu, D. Cao, P. Wang, G. Wang, Y. Gao, Int. J. Hydrogen. Energy 36 (2011) 72–78.
[4] V. Rashkova, S. Kitova, I. Konstantinov, T. Vitanov, Electrochim. Acta 47 (2002) 1555–1560.
[5] F. Song, L. Bai, A. Moysiadou, et al., J. Am. Chem. Soc. 140 (2018) 7748–7759.
[6] H. Qiao, J. Yong, X. Dai, et al., J. Am. Chem. Soc. 5 (2017) 21320–21327.
[7] J. Suntivich, K.J. May, H.A. Gasteiger, J.B. Goodenough, Y. Shao-Horn, Science 334 (2011) 1383–1385.
[8] A. Grimaud, O. Diaz-Morales, B. Han, et al., Nat. Chem. 9 (2017) 457–465.
[9] J. Zhang, Z. Zhao, Z. Xia, L. Dai, Nat. Nanotechnol. 10 (2015) 444–452.
[10] T. Reier, M. Oezaslan, P. Strasser, ACS Catal. 2 (2012) 1765–1772.
[11] S. Park, Y. Shao, J. Liu, Y. Wang, Energy Environ. Sci. 5 (2012) 9331–9344.
[12] Y. Zheng, Y. Jiao, Y. Zhu, et al., J. Am. Chem. Soc. 138 (2016) 16174–16181.
[13] H. Sun, Z. Yan, F. Liu, et al., Adv. Mater. 32 (2020) 1806326.
[14] U.Y. Qazi, C.Z. Yuan, N. Ullah, et al., ACS Appl. Mater. Interface 9 (2017) 28627–28634.
[15] N.T. Suen, S.F. Hung, Q. Quan, et al., Chem. Soc. Rev. 46 (2017) 337–365.
[16] Y. Liu, H. Wang, D. Lin, et al., Energy Environ. Sci. 8 (2015) 1719–1724.
[17] Z. Liu, X. Yu, H. Yu, H. Xue, L. Feng, ChemSusChem 11 (2018) 2703–2709.
[18] M.E.G. Lyons, M.P. Brandon, J. Electroanal. Chem. 641 (2010) 119–130.
[19] P. Rüetschi, P. Delahay, J. Chem. Phys. 23 (1955) 556–560.
[20] M.S. Burke, L.J. Enman, A.S. Batchellor, S. Zou, S.W. Boettcher, Chem. Mater. 27 (2015) 7549–7558.
[21] J. Rossmeisl, Z.W. Qu, H. Zhu, G.J. Kroes, J.K. Nørskov, J. Electroanal. Chem. 607 (2007) 83–89.
[22] Y. Li, H. He, W. Fu, et al., Chem. Commun. 52 (2016) 1439–1442.
[23] M.W. Louie, A.T. Bell, J. Am. Chem. Soc. 135 (2013) 12329–12337.
[24] L. Trotochaud, S.L. Young, J.K. Ranney, S.W. Boettcher, J. Am. Chem. Soc. 136 (2014) 6744–6753.
[25] M. Gong, Y. Li, H. Wang, et al., J. Am. Chem. Soc. 135 (2013) 8452–8455.
[26] S. Yin, W. Tu, Y. Sheng, et al., Adv. Mater. 30 (2018) 1705106.
[27] H. Li, S. Liang, J. Li, L. He, J. Mater. Chem. A 1 (2013) 6335–6341.
[28] G. Wang, J. Yang, J. Park, et al., J. Phys. Chem. C 112 (2008) 8192–8195.
[29] S. Fang, D. Huang, R. Lv, et al., RSC Adv. 7 (2017) 25773–25779.
[30] K. Krishnamoorthy, M. Veerapandian, R. Mohan, S.J. Kim, Appl. Phys. A 106 (2012) 501–506.
[31] P. Nakhanivej, X. Yu, S. Park, et al., Nat. Mater. 18 (2019) 156–162.
[32] C. Wang, H. Yang, Y. Zhang, Q. Wang, Angew. Chem. Int. Ed. 58 (2019) 6099–6103.
[33] T. Ma, M. Yuan, S.M. Islam, et al., J. Alloys. Compd. 678 (2016) 468–477.
[34] Z. Wang, J. Li, X. Tian, et al., ACS Appl. Mater. Inter. 8 (2016) 19386–19392.
[35] H. Shin, H. Xiao, W.A. Goddard, J. Am. Chem. Soc. 140 (2018) 6745–6748.
[36] J.T. Ren, G.G. Yuan, C.C. Weng, L. Chen, Z.Y. Yuan, Nanoscale 10 (2018) 10620–10628.
[37] Y. Xue, Y. Wang, H. Liu, et al., Chem. Commun. 54 (2018) 6204–6207.